Title
Identifying Strain Stacking Boundaries between Multiphase Domains in Atomically Thin Two-Dimensional Magnets

Journal
ACS Nano, 20(11)

ISSN
1936-0851

Authors
Bhusal, Hem Prasad
Tanaka, Koichi
Zeltmann, Steven
et al.

Publication Date
2026-03-24

DOI
10.1021/acsnano.5c14666

Identifying strain stacking boundaries between multi-phase domains in atomically thin two-dimensional magnets

Hem Prasad Bhusal[†], Koichi Tanaka[†], Steven Zeltmann[¶], Chris Hanley[&], Colin Ophus[Λ,‡], Karen C. Bustillo[‡], Stephanie M. Ribet[‡], Carlos Gonzalez[†], Belinda Zhen[†], Jim Ciston[‡], Zhehao Ge[†], Jason C. Lashley[§], Alex K. Zettl[ǀ], Jairo Velasco Jr.[†], Wei Chen[&], Aiming Yan[†,*]

[†] Physics Department, University of California, Santa Cruz, CA, 95064, USA

[¶] Department of Materials Science and Engineering, University of California, Berkeley, CA, 94720, USA

[Λ]Department of Materials Science and Engineering, Stanford University, Palo Alto, CA, 94305, USA

[‡] National Center for Electron Microscopy, Molecular Foundry, Lawrence Berkeley National Laboratory, Berkeley, CA, 94720, USA

[§] Savannah River National Laboratory, Jackson, SC, 29831, USA

[&] Department of Materials Design and Innovation, University at Buffalo, Buffalo, NY, 14260, USA

[ǀ] Physics Department, University of California, Berkeley, CA, 94720, USA

[*] Corresponding author: aiyan@ucsc.edu

Abstract:

Stacking engineering of van der Waals materials is an important strategy to control the materials' properties, such as electronic correlations, ferroelectricity and layer-dependent two-dimensional magnetism. A timely testbed for the study of the latter is atomically thin chromium trihalides (CrX_3,

X= Cl, Br, I). Notably, by understanding the sliding mechanism between different stacking sequences, control of the stacking arrangement and thus magnetic properties in CrX_3 can be achieved. Such insight, however, is currently lacking. Here, advanced electron microscopy methods are used to identify multiple stacking sequences corresponding to different bulk phases in atomically thin CrX_3 (X= Cl and Br) down to bilayer thickness and with lateral domain sizes as small as tens of nanometers. Indications of nanometer scale transitions and interactions at the stacking boundaries are found, including a universally preferred sliding direction that is consistent with density functional theory calculations and the strain fields at lateral heterostructure boundaries. This study demonstrates the necessity to consider local stacking structures when interpreting averaged magnetic properties measured with macroscale probes. Additionally, the preferred sliding direction insight from this study provides a strategy to control stacking sequence in atomically thin CrX_3 samples during the exfoliation and sample fabrication process.

Keywords: two-dimensional magnetism; magnetic properties; four-dimensional scanning transmission electron microscopy; stacking engineering; DFT calculations.

Stacking control in van der Waals materials has fundamental importance as the stacking sequence is known to dictate the materials' properties such as strongly correlated physics in rhombohedral stacked multilayer graphene[1,2] and magic-angle twisted van der Waals heterostructures.[3–7] To realize stacking control, it is essential to understand the sliding behavior in van der Waals materials. Stacking boundaries are the key structural elements that significantly impact this sliding behavior. For example, the stacking boundaries between AB and BA stacked domains in bilayer graphene are strain solitons and have a cross-boundary sliding direction along

the armchair edge of the honeycomb lattice of carbon.[8] In addition, in-situ experimental studies show that room-temperature mechanical stimulation is sufficient to cause the migration of these stacking boundaries.[9–11] The preferred sliding direction combined with the effectiveness of mechanical stimulation to manipulate the stacking sequence leads to a more accessible strategy to maximize the domain size with rhombohedral stacking in multilayer graphene.[12] This strategy aims to align the shear force during the stack assembly with the zig-zag direction of the honeycomb lattice to avoid undesired interlayer sliding. Similar strategies can potentially be applied to other van der Waals materials to realize manipulation of their stacking sequence.[13]

Another important example of stacking-dependent properties occurs in two-dimensional (2D) magnets[14–17] such as chromium trihalides (CrX_3, X=Cl, Br, and I), where tunable[18–22] and layer-dependent magnetism can be realized via stacking engineering.[17,23–27] 2D magnets hold promises for spintronic applications, potentially leading to next-generation low-power electronics and quantum computing.[28–30] 2D magnets also provide opportunities for the development of highly integrated, flexible, and biocompatible devices and sensors based on magnetic effects.[31,32] To achieve control over magnetic properties in CrX_3, manipulation of the stacking sequence becomes essential, and a first step towards this goal is to understand the interlayer sliding behavior between different stacking sequences in these materials.

Previous studies have shown that the exfoliation process- a typical method to prepare atomically thin van der Waals materials can significantly impact the stacking structure of CrX_3. More specifically, the exfoliation process freezes the stacking sequence corresponding to the stable phase of bulk CrX_3 at room temperature, at which the exfoliation takes place.[33] Furthermore, unlike bulk CrX_3, which undergoes phase transition from high-temperature monoclinic phase to low-temperature rhombohedral phase,[34,35] the exfoliated thin CrX_3 does not undergo any phase

transition at low temperatures.[24,25,34,36–38] The lack of phase transition in thin CrX_3 is manifested as an unchanged stacking sequence below the phase transition temperature, and consequently leads to magnetic properties different from its bulk counterpart.[24,25,33,34,36–38]

Although the above studies reveal a dominant stacking sequence, it is not clear whether complicated domain structures exist in exfoliated thin CrX_3 at the sub-micron or even nanometer scale. Macroscale magnetic property and structural characterization show the existence of mixed phases in bulk and exfoliated CrX_3.[26,27,39] However, these characterization techniques such as SQUID (superconducting quantum interference device) magnetometry combined with X-ray diffraction,[39] tunneling magnetoresistance measurements,[26,27] second-harmonic generation[33] and Raman spectroscopy[24] have limited spatial resolutions at around or greater than 1 micrometer. A higher resolution characterization tool is needed to study the detailed domain and boundary structures to reveal the sliding behavior in exfoliated few-layer CrX_3.

Here, we use four-dimensional scanning transmission electron microscopy (4D-STEM) in the plane-view sample geometry to study the stacking structure at the nanometer scale in exfoliated atomically thin CrX_3 (X= Br and Cl) encapsulated between two sheets of few-layer graphene (Fig. S1). Because CrX_3 is extremely sensitive to air and moisture,[24,37,40] both the exfoliation and encapsulation processes are performed in an inert environment (a glovebox filled with argon or nitrogen gas). Although our samples have few-layer graphene capping layers, which usually obscure contrast under imaging modes, the spatially resolved diffraction patterns acquired in 4D-STEM can easily separate the reflections from the capping layers and those from the CrX_3, thus providing unambiguous structural information of the target material. We also find that 4D-STEM, equipped with highly efficient direct electron detectors and optimized acquisition parameters, often enables characterization at a dose that helps minimize beam damage to the atomically thin

CrX_3 samples. We choose $CrBr_3$ and $CrCl_3$ as the representative cases (with the focus on $CrCl_3$) because they possess different stacking sequences at room temperature when being exfoliated.

Our study reveals that monoclinic and rhombohedral stacking sequences can co-exist in exfoliated bi- and tri-layer $CrCl_3$ and trilayer $CrBr_3$, and the stacking boundaries usually connect domains with a dominant stacking sequence and a minor stacking sequence. We identify that these stacking boundaries are strain boundaries and have rich strain structures via 4D-STEM characterization. A recent pioneering cross-sectional TEM study reveals twisted monoclinic domain structures in exfoliated and non-exfoliated bulk CrI_3, and that the exfoliation process reduces the single-domain thickness by an order compared to non-exfoliated bulk counterpart.[41] However, the in-plane domain structure was inaccessible in a cross-sectional characterization, not to mention the detailed stacking boundary structure that is key to understanding the sliding behavior. In our 4D-STEM in-plane approach, we identify the preferred sliding direction at the stacking boundaries to be along the zig-zag direction of the Cr lattice. This experimental observation is consistent with density functional theory (DFT) calculations and provides insight into a potential strategy to realize stacking control in exfoliated thin CrX_3.

Results and Discussion

Identification of monoclinic stacking (M stacking) and rhombohedral stacking (R stacking) in bilayer $CrCl_3$

As shown in Figure 1a, single-layer CrX_3 has a primitive structure of hexagonal lattice with D_{3d} point group symmetry and P-31m space group symmetry.[15,42] Each layer of CrX_3 is composed of three layers of atoms, with one layer of Cr atoms sandwiched between two layers of halogen atoms (X). We use hexagons to outline the Cr atoms, solid triangles to distinguish the top X atoms, and dashed triangles to distinguish the bottom X atoms. In the rest of the paper, we simply use

hexagons with or without triangles to represent bi- and tri-layer CrX_3 with different stacking sequences. Bilayer CrX_3 with the stacking sequence corresponding to the monoclinic phase (or M stacking) and the rhombohedral phase (or R stacking) of bulk CrX_3 are shown in Figure 1b (with additional schematics for the bulk CrX_3 structure in both phases in Fig. S3). The stacking sequence in bilayer CrX_3 is determined by the in-plane displacement vector $\boldsymbol{u}$ between the two layers, and these two layers have the same orientation (or chirality[15]) for exfoliated CrX_3 samples. The in-plane displacement for M-stacked bilayer CrX_3–$\boldsymbol{u_m}$ is along the zig-zag direction of the Cr lattice and $|\boldsymbol{u_m}| = \frac{1}{3}a_0$ (a_0 is the lattice constant for single-layer CrX_3). To satisfy the close-packing condition,[15] only three equivalent displacement vectors (arrows in Figure 1b) that are $120°$ rotated from each other are allowed for M stacking. For R-stacked bilayer CrX_3, the in-plane displacement vector $\boldsymbol{u_r}$ is along the armchair direction of the Cr lattice and $|\boldsymbol{u_r}| = \frac{\sqrt{3}}{3}a_0$. Six equivalent displacement vectors that are rotated by $60°$ between the neighboring two vectors are allowed for R stacking as shown in Figure 1b.

Here we focus on bilayer and trilayer CrX_3 samples to unambiguously reveal the details of the stacking structures especially at the boundaries. To determine the thickness and thus the number of layers of exfoliated CrX_3 samples, we use an atomic force microscope located in the glovebox to measure the thickness after exfoliation and before encapsulation of CrX_3. An example of exfoliated bilayer $CrCl_3$ is shown in Figure 1c, with a measured thickness of ~1.2 nm, consistent with other work.[24,43] It is well known that like other 2D materials the thickness of thin CrX_3 with a certain layer number measured by atomic force microscopy can fluctuate[17,24,43,44] due to the surface roughness of the SiO_2/Si substrate[45] and the experimental conditions of the atomic force microscope.[46] We consider the possible variation of layer number estimated from the initial atomic force microscopy measurement and further determine the exact layer number during the TEM

study detailed below. To improve the accuracy of layer number estimation, we statistically investigate the average thickness of thin CrX_3 of a certain layer number that has been confirmed by TEM. An example of such investigation to obtain the average thickness for bilayer $CrCl_3$ samples ($1.194 \pm 0.035nm$) is shown in Figure S4.

Bilayer CrX_3 with the M stacking and R stacking have different crystal symmetry that can be detected via electron diffraction. As shown in Figure 1d, 4D-STEM uses a nanometer-sized (or even sub-nm-sized) electron beam to scan across a large sample area (ranging from hundreds of nanometers to micrometers), and at each scan point a convergent beam electron diffraction (CBED) pattern is collected and provides structural information at that point.[47] This is different from other scanning electron diffraction techniques such as low energy electron diffraction (LEED). LEED uses a low energy (typically 20-200 eV), large (~ 0.5-1 mm) nearly parallel electron beam to scan the surface of a material and collects backscattered electrons that characterize the crystal structure of the first few atomic layers of the material.[48] The surface sensitivity of LEED makes it unsuitable for studying air-sensitive samples that need capping layers like those in our work. In addition, because of the large beam size used in LEED, it cannot provide nanoscale structural information of a material. By using 4D-STEM, we can identify different stacking sequences from local positions and obtain detailed structural information from the stacking boundaries.

In Figure 1d, two representative experimental CBED patterns from the regions of M-stacked (left) and R-stacked (right) bilayer $CrCl_3$ show two families of prominent diffraction spots: diffraction peaks d (highlighted with blue circles), and diffraction peaks d' (highlighted with blue squares). Diffraction peaks d correspond to a lattice line periodicity of $a = a_0$ while diffraction peaks d' correspond to a shorter lattice line periodicity of $a' = \frac{1}{3}a_0$. All d and d' peaks correspond to lattice lines along the zig-zag directions of the Cr lattice. By comparing the symmetry in the

experimental CBED patterns with that in the simulated diffraction patterns based on multi-slice method (Figures S5 and S6), we can determine the stacking sequence observed in our experiments.

It is worth noting that single-layer $CrCl_3$ possesses six-fold symmetry originated from its hexagonal lattice structure. This six-fold symmetry is maintained in R-stacked bilayer $CrCl_3$ due to the intrinsic six-fold symmetry of the equivalent in-plane displacement vectors as shown in Figure 1b. In contrast, such a six-fold symmetry is broken in M-stacked bilayer $CrCl_3$ because the three equivalent in-plane displacement vectors for M-stacking possess three-fold instead of six-fold symmetry. Therefore, the diffraction pattern from R-stacked bilayer $CrCl_3$ has six-fold symmetry while the diffraction pattern from M-stacked bilayer $CrCl_3$ has two-fold symmetry. In the experimental CBED pattern corresponding to the M-stacked bilayer $CrCl_3$ in Figure 1d, four of the d peaks have similar intensities and are weaker than the other two d peaks (one of which is blocked by the beam stop). All five d' peaks have similar intensities (the sixth d' peak is blocked by the beam stop). In the experimental CBED pattern corresponding to the R-stacked bilayer $CrCl_3$, all five d peaks have similar intensities and all five d' peaks have similar intensities. These observations are consistent with the simulated electron diffraction pattern from M-stacked bilayer $CrCl_3$ and R-stacked bilayer $CrCl_3$, respectively (Figures S5 and S6). The no-marker version of CBED patterns in Figure 1d is provided in Figure S2 for better visual comparison.

The quantitative comparison of the relative intensity of the diffraction peaks can be understood by considering the relative phase shift (θ) between the two layers, which is the foundation of the interference theory. Other factors such as sample tilt also need to be considered for more accurate quantitative comparison (see Section 2.2 in the Supporting Information). Initial characterization via electron diffraction confirms that the dominant stacking sequence in exfoliated

bilayer and trilayer $CrCl_3$ at room temperature is the M stacking, corresponding to the monoclinic phase (Section 1 in the Supporting Information).

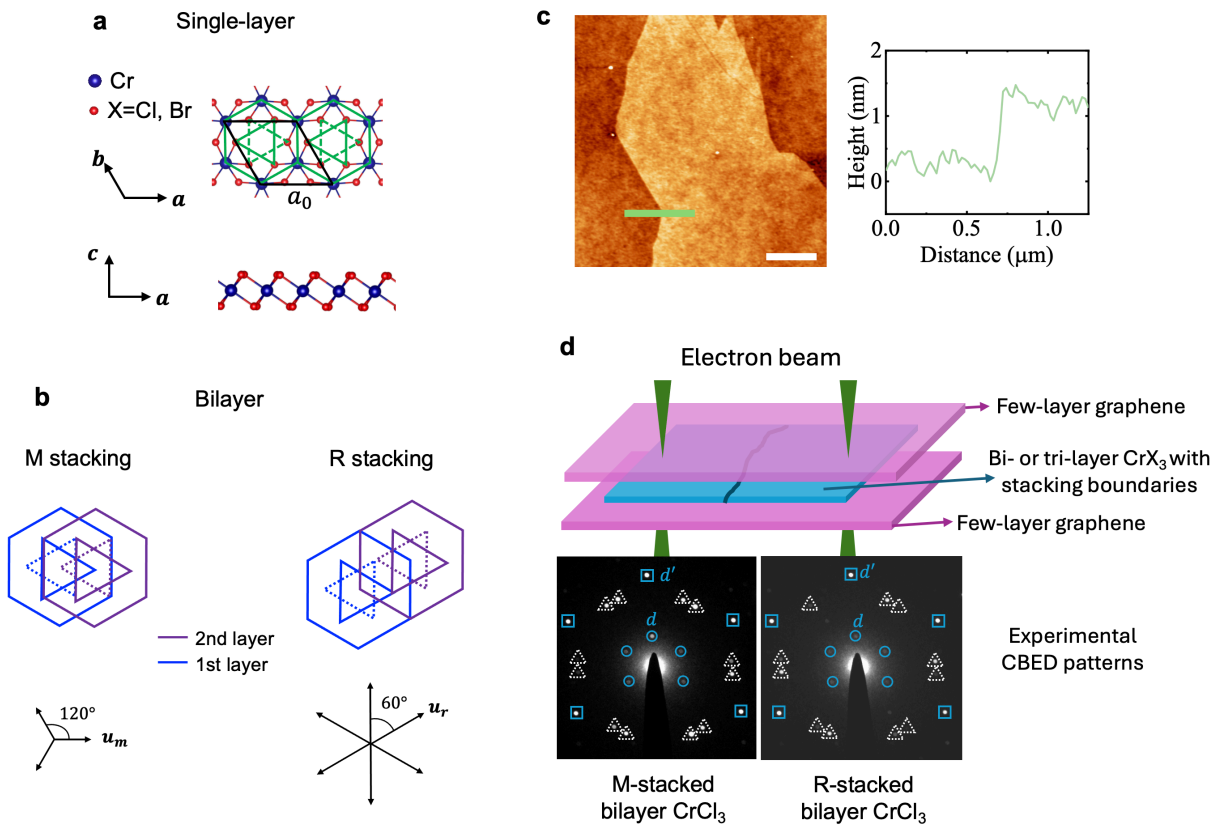

Figure 1: Characterization of atomically thin CrX_3 using 4D-STEM. *(a) Schematics of the top view and side view of single-layer* CrX_3 *(X=Cl and Br). Green hexagons outline the Cr lattice. Green solid triangles outline the X lattice in the top layer of single-layer* CrX_3*, while the dashed triangles outline the X lattice in the bottom layer. A unit cell is indicated in black solid lines with a lattice constant* a_0*.(b) Schematics for the top view of bilayer* CrX_3 *with M stacking and R stacking. The interlayer displacement vectors for variant M stackings and R stackings are indicated below the atomic structures. (c) Atomic force microscopy height image of bilayer* $CrCl_3$ *flake exfoliated onto a* SiO_2/Si *substrate. A height profile of the* $CrCl_3$ *flakes along the green line is shown on the right. Scale bar is 1 μm. (d) Schematic of 4D-STEM to study domains with different stacking sequences and the stacking boundaries in bilayer and trilayer* CrX_3 *encapsulated in two*

sheets of few-layer graphene. The representative experimental CBED patterns correspond to the M stacking and R stacking of bilayer $CrCl_3$. Diffraction peaks belonging to d and d' families for bilayer $CrCl_3$ are highlighted in blue circles and squares respectively, while the diffraction peaks for the two few-layer graphene sheets in white triangles.

Preferred sliding direction at the stacking boundaries between a dominant M-stacked domain and a minor R-stacked domain in bilayer $CrCl_3$

In addition, our 4D-STEM studies reveal that variant M-stacking sequences exist in exfoliated bilayer $CrCl_3$ and these domains with the dominant stacking sequence are connected by domains with the minor stacking sequence- R stacking. Figure 2 shows a typical bilayer $CrCl_3$ sample that has such complicated domain structures. We use M_n (n=1, 2, and 3) to represent the three variant M stackings with the interlayer displacement vector $\boldsymbol{u_m}$ that is 120° rotated from each other, and R_n (n=1-6) to present the six variant R stackings with $\boldsymbol{u_r}$ that is 60° rotated from each other. By analyzing 4D-STEM data, especially virtual dark-field images of these bilayer $CrCl_3$ samples, we can obtain structural information from a given domain. Figure 2a shows a typical CBED pattern from one scan spot with M stacking (randomly assigned as M_1), which has one strong d peak (d_3 in Figure 2a, the other symmetric peak is blocked by the beam stop) and four weak d peaks. The strong d_3 peak corresponds to the lattice line direction along the in-plane displacement vector for M_1 stacking $\boldsymbol{u_{m_1}}$. A comparison in intensity of the five d peaks is shown in Figure S7, which is consistent with the simulated diffraction pattern of bilayer $CrCl_3$ with M stacking (Section 2 in the Supporting Information). The virtual dark-field image from the d_3 peak highlights the domain with M_1 stacking (Figure 2b), while the virtual dark-field image from d_1 peak shows the domain with M_2 stacking in brighter contrast (Figure 2c). Based on the relative intensities of d peaks

(Figure S7 and Section 2 in the Supporting Information), we can also identify the domains with R stackings assigned as R_1 and R_2, indicated in Figure 2c.

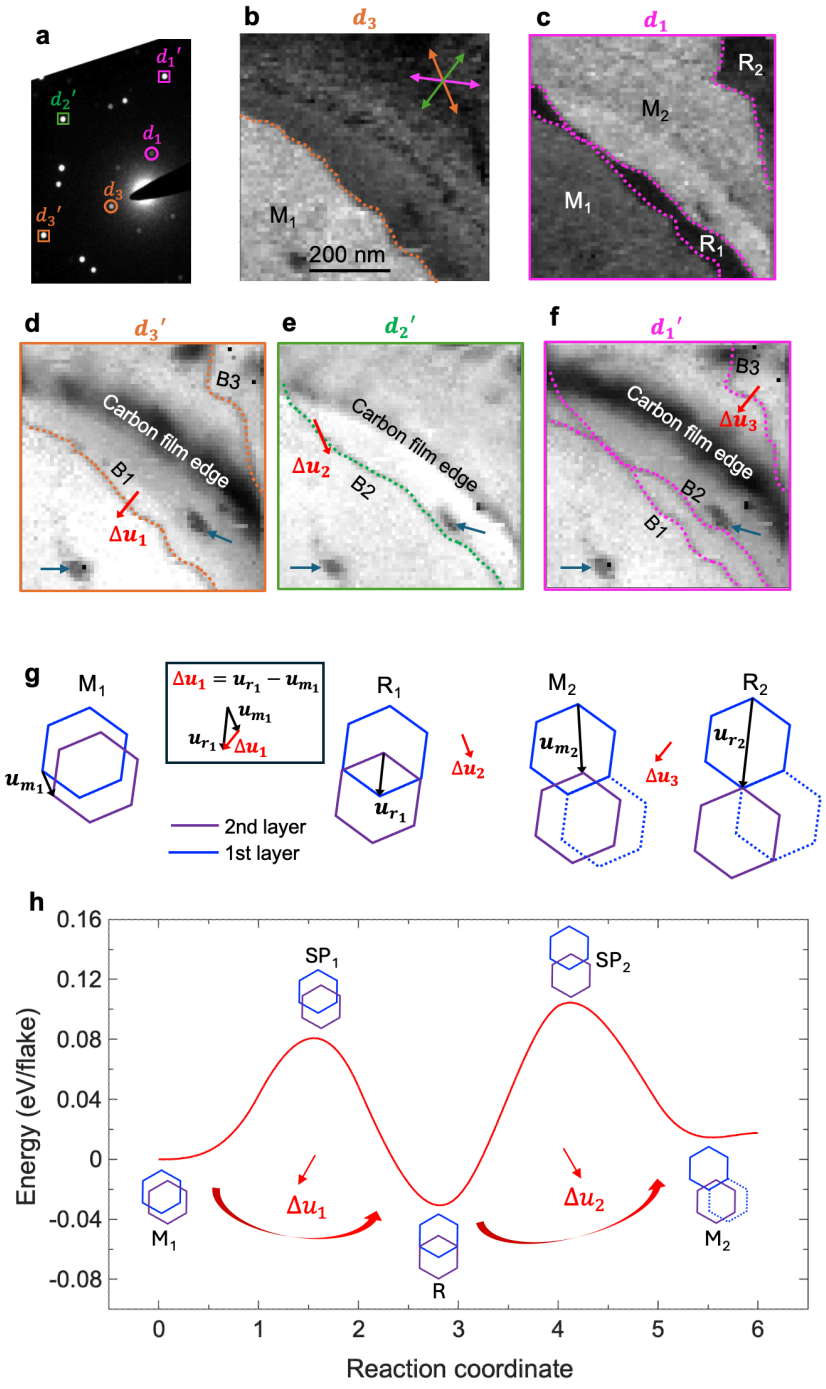

***Figure 2: Domains with the dominant M-stacking and the minor R-stacking in bilayer* $CrCl_3$.** *(a) A typical CBED pattern from the 4D-STEM data collected from the area assigned as M_1*

stacking in b. The two d peaks are circled in magenta and orange respectively, while the three d' peaks are boxed and color-coded according to the main reciprocal directions. (b) Virtual dark-field image from d_3 peak, showing the M_1 stacked region in brighter contrast compared to the rest of the area. (c) Virtual dark-field image from d_1 peak, showing the M_2 stacked region in brighter contrast compared to the rest of the area. (d)-(f), Virtual dark-field images from three d' peaks, showing the three stacking boundaries B_1, B_2 and B_3. The edge of the hole in the carbon film on the TEM grid is indicated. Scale bars in (b)-(f) are the same. Virtual dark-field images formed from d peaks are plotted under the same color scale while virtual dark-field images formed from d' peaks are plotted under the same color scale. This applies for all virtual dark-field images shown in the rest of the paper. The direction of the translation vector at each boundary is indicated by a red arrow. (g) Schematics of two variant stacking structures corresponding to each of the two phases existing in the sample. The color of each layer is indicated. (h) DFT CI-NEB calculations to identify the MEP for the transition between two variant M-stackings of bilayer $CrCl_3$.

Virtual dark-field images from d' peaks provide additional structural information on the stacking boundaries based on the interference theory (Section 2 in the Supporting Information). We note that certain stacking boundaries appear in the virtual dark-field images from two sets of the d' peaks but disappear in that from the third set as shown in Figure 2d-f. For example, the stacking boundary between M_1 and R_1 (denoted as B_1) appears in the virtual dark-field images from d_3' and d_1' peaks but disappears in the virtual dark-field image from d_2' peak. This indicates that at this stacking boundary the translation vector $\Delta\boldsymbol{u_1}(=\boldsymbol{u_{r_1}}-\boldsymbol{u_{m_1}})$ is exactly along the direction corresponding to d_2' peak (also indicated by the green arrow in Figure 2b) and satisfies the fully constructive interference condition.

By using the same method, we can determine the direction for $\Delta \boldsymbol{u_n}$ at all three stacking boundaries indicated by a red arrow in Figure 2d-f, respectively. The direction of the translation vector $\Delta \boldsymbol{u_n}$ is also the sliding direction from one stacking sequence to the other one across the stacking boundary. We find that the sliding direction at each boundary is 60° rotated from that at the neighboring boundary. We then determine $\boldsymbol{u_{m_1}}$ for the M_1 stacking, which is perpendicular to the reciprocal direction of the strong peak d_3 and indicated by the orange arrow in Figure 2b. Based on $\boldsymbol{u_{m_1}}$ and the direction of $\Delta \boldsymbol{u_1}$ we can determine $\boldsymbol{u_{r_1}}$ for R_1 stacking assuming the first layer is continuous across the boundary. Applying the same method, we can determine $\boldsymbol{u_{m_2}}$ for M_2 stacking and $\boldsymbol{u_{r_2}}$ for R_2 stacking (Figure 2g). We find that all three stacking boundaries observed here have a preferred sliding direction (the direction of the translation vector $\Delta \boldsymbol{u_n}$) along one of the zig-zag directions of the honeycomb lattice of Cr, and the magnitude of the sliding path at all three boundaries is $\frac{1}{3}a_0$. Although the translation vector can potentially adopt different magnitude (Figure S8), we assume the shorter the translation across the boundary the more energetically favorable. This is further confirmed via DFT calculations.

Since our experimental observation involves two variant M-stacking sequences in bilayer $CrCl_3$, we perform first-principles climbing image nudged elastic band (CI-NEB) calculations[49] to determine the minimum energy pathway (MEP) for the $CrCl_3$ flake to slip between the two variant M-stacking configurations. As shown in Figure 2h, these two configurations denoted as M_1 and M_2 serve as the initial and final states. Owing to typical DFT-level uncertainties, there is a minor energy difference of 1.1×10^{-4} eV/atom between them. Geometrically, the M_1 stacking can turn into the M_2 stacking by laterally shifting the top layer by $\frac{\sqrt{3}}{3}a_0$ along one of the armchair directions of the Cr lattice, and this direct, linear slip would seem like the simplest path. However,

interestingly, the MEP involves an intermediate R-stacking configuration, which is a global minimum in the energy landscape as shown in Figure 2h. The energy barrier for this transition from M_1 to R stacking is approximately 0.102 eV per $CrCl_3$ flake (or about 0.013 eV per $CrCl_3$ unit) and the saddle point SP_1 occupies the highest energy point along the transition pathway. The sliding direction during this transition is along one of the zig-zag edges of the Cr lattice and has magnitude of $|\Delta \boldsymbol{u_1}| = \frac{1}{3}a_0$, which is consistent with our experimental observations. The transition from the R stacking to M_2 stacking involves a similar energy barrier with a sliding direction also along one of the zig-zag edges of the Cr lattice that is rotated by 60° relative to the translation vector for the M_1 to R transition. The translation vector $\Delta \boldsymbol{u_2}$ has magnitude of $\frac{1}{3}a_0$, the same as that for M_1 to R transition.

All the above results from DFT calculations (Section 7 in the Supporting Information) are consistent with our experimental observations. The relatively low barrier suggests that the monoclinic-to-rhombohedral transition can be facilitated by thermal fluctuations or mechanical stimuli, such as shear force during exfoliation and stack assembly processes. These findings indicate that transitions between monoclinic and rhombohedral stackings are significantly more accessible than transitions within purely monoclinic or rhombohedral configurations, and this may explain why we only observe stacking boundaries between M stacking and R stacking (or another minor stacking sequence as discussed below) in few-layer $CrCl_3$.

Stacking boundaries between an M-stacked domain and an R-stacked domain with similar sizes

Besides the case shown in Figure 2 where nanometer-sized regions with the minor R stacking are embedded in the dominant M-stacked regions, we also observe the coexistence of R-stacked and M-stacked regions with similar sizes (as shown in Figure 3). In the bilayer $CrCl_3$ case (Figure 3a-

d), from the symmetry of the diffraction pattern in Figure 3a, we confirm that part of the sample is an M-stacked region, which has a bright contrast in the virtual dark-field image from diffraction peak d_1 (Figure 3b). The stacking boundary appears in the virtual dark-field images from d_1' and d_3' peaks and is invisible in the virtual dark-field image from d_2' peak (Figure 3c and d). Using the same method discussed above, we can determine the in-plane displacement for both R- and M-stackings and the translation vector $\Delta\boldsymbol{u}$ across the boundary. We find that the translation vector has the direction along one of the zig-zag directions of the Cr lattice and magnitude of $\frac{1}{3}a_0$, consistent with the bilayer case in Figure 2. Blue arrows in Figure 3c and d point to defects most likely due to partial degradation. The defect clusters at the end of the stacking boundary are speculated to be the pinning points for this boundary and to stabilize the R-stacked region, which is less stable than an M-stacked region at room temperature for $CrCl_3$.[15]

Stacking boundaries between an R-stacked region and an M-stacked region with similar sizes can also occur in trilayer $CrCl_3$. One example of trilayer $CrCl_3$ with such a stacking boundary is presented in Figure 3e-j. Figure 3e shows a typical CBED pattern from the region with a stacking sequence that is different from a pure M-stacking or a pure R-stacking, where "pure" means the two $\boldsymbol{u}$ vectors between adjacent layers are the same. This diffraction pattern has four d peaks with equal intensities and the other two are absent. This unique symmetry indicates this area is neither pure M-stacking nor pure R-stacking (see simulated diffraction patterns in Figures S5 and S6), Besides pure M-stacking and pure R-stacking, there are three other possible stacking sequences that are energetically favorable for a trilayer $CrCl_3$ speculated based on DFT calculations:[18] 1) a mixture of variant M-stackings; 2) a mixture of variant R-stackings; 3) a mixture of M-stacking and R-stacking. Based on the interference theory and simulated diffraction patterns of the above possible stacking sequences (Figures S5, S6 and S9), the only plausible stacking sequence that can

lead to the symmetry shown in this diffraction pattern is the third scenario– a mixture of M-stacking and R-stacking. We use M+R to represent this mixed stacking (see a detailed discussion in Section 3 in the Supporting Information). The rest of the area shows diffraction patterns with symmetry the same as Figure 3f, where two strong d peaks occur and the other four d peaks are absent. By comparing the experimental pattern to the simulated diffraction patterns for trilayer $CrCl_3$ with different stacking sequences (Figures S5, S6 and S9), we conclude that this diffraction pattern corresponds to pure M stacking.

To obtain more structural information at the stacking boundaries, we investigate virtual dark-field images. A virtual dark-field image from the d_2 peak (in Figure 3e or f) shows the M-stacked region in brighter contrast (Figure 3g), and the region with a mixed stacking sequence of M- and R-stacking in darker contrast (see Section 3 in the Supporting Information). By investigating virtual dark-field images from the d' peaks, we obtain additional information about the stacking boundary in this trilayer sample. The stacking boundary appears in virtual dark-field images from $d_2{}'$ and $d_3{}'$ (Figure 3h) and disappears in the virtual dark-field image from $d_1{}'$ (Figure 3i). This indicates that the translation vector $\boldsymbol{\Delta u}$ across the boundary is exactly along the lattice line direction corresponding to the reciprocal direction of $d_1{}'$, which is along the zigzag direction of the Cr lattice as indicated by the magenta arrow in Figure 3g. The magnitude of $\boldsymbol{\Delta u}$ is determined as $\frac{1}{3}a_0$, consistent with all the other stacking boundaries observed so far. Based on the above information, we can determine the atomic structure of the mixed M+R stacking and pure M-stacking as shown in Figure 3j. It is worth noting that a possible observation of a mixture of M- and R-stacking has been reported in trilayer $CrCl_3$ by using Raman spectroscopy at low temperatures.[24] Notably, unlike Raman spectroscopy, which has limited spatial resolution, our

study uses 4D-STEM to shed light into the nanoscale structural information at the stacking boundaries involving such mixed stacking sequences.

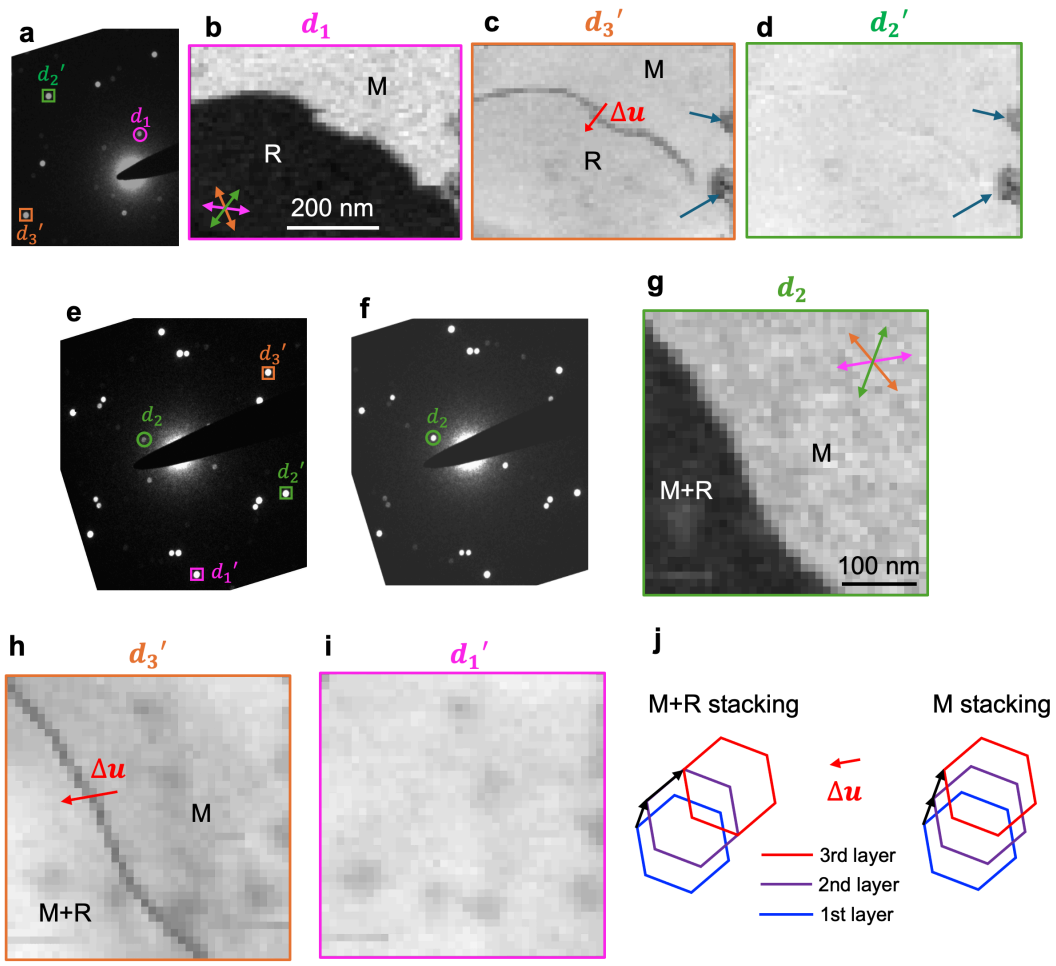

Figure 3: Stacking boundaries between an R-stacked region and an M-stacked region with similar sizes in bilayer and trilayer $CrCl_3$. *(a)-(e): Stacking boundary between an R-stacked region and an M-stacked region with similar sizes in bilayer* $CrCl_3$. *(a) A typical CBED pattern from the M-stacked region indicated in (b). (b) Virtual dark-field image from* d_1 *peak. (c) Virtual dark-field image from* d_3' *peak, showing the stacking boundary. The direction for the translation vector across the boundary is indicated by a red arrow. (d) Virtual dark-field image from* d_2' *peak, where the stacking boundary is invisible. Blue arrows in (c) and (d) point to the defect clusters.*

Scale bars in (b)-(d) are the same. (e)-(j), Stacking boundary between an R-stacked region and an M-stacked region with similar sizes in trilayer $CrCl_3$. *(e) and (f), Typical CBED patterns from the area with the M+R stacking, and the area with the M-stacking in trilayer* $CrCl_3$, *respectively. (g) Virtual dark-field image from* d_2 *peak in (e) or (f). Real space directions corresponding to the main diffraction peaks are shown in color-coded arrows. (h) and (i), Virtual dark-field images from one of the* d' *peaks (*d_3' *and* d_1'*, respectively). The red arrow in (h) indicates the direction of the translation vector* $(\Delta \boldsymbol{u})$ *across the boundary. Scale bars for (g)-(i) are the same. (j) Schematics of the mixed stacking sequence of M+R stacking on the left and the pure M-stacking of trilayer* $CrCl_3$ *on the right.*

Similar boundary structure in atomically thin $CrBr_3$

Such stacking boundaries between M- and R-stacked regions not only exist in exfoliated atomically thin $CrCl_3$ but also in exfoliated atomically thin $CrBr_3$. However, unlike $CrCl_3$, bulk $CrBr_3$ has a phase transition temperature above room temperature and possesses the rhombohedral phase at room temperature.[34,50] This means thin $CrBr_3$ exfoliated at room temperature adopts the dominant R-stacking. In our 4D-STEM studies on exfoliated trilayer $CrBr_3$, we identify stacking boundaries that connect M-stacked and R-stacked domains (where the R-stacked domains are dominant as shown in Fig. S13), and the stacking boundaries also have a preferred sliding direction along the zigzag direction of the Cr lattice (see Section 4 in the Supporting Information). Notably, this preferred sliding direction at the stacking boundaries in $CrBr_3$ is the same as that observed in $CrCl_3$. The potential universality of this phenomenon in CrI_3 requires future systematic studies as presented in this work.

Strain fields at a stacking boundary in trilayer $CrCl_3$

Besides the above observed various stacking sequences based on the two most stable stacking sequences– R-stacking and M-stacking, we also observe a rare stacking sequence called A-stacking that occupies another local minimum in the energy landscape.[15] This A-stacking sequence has a slightly higher energy than the M-stacking and occurs in one of our trilayer $CrCl_3$ samples. The schematic of trilayer $CrCl_3$ with an AA-stacking sequence is shown on the left of Figure 4a, where all three layers are overlapped with each other. A typical CBED diffraction pattern from the AA-stacked region has six strong d peaks due to the perfect constructive interference among the three layers (Figure S14a). These strong peaks have a similar intensity as that of the two strong d peaks in the region on the opposite side of the stacking boundary in this tri-layer $CrCl_3$ sample (Figure S14b). Based on the symmetry of the diffraction patterns from this region and the interference theory, we deduce the stacking order in this area is a mixture of A- and M-stacking (or A+M stacking as shown in Figure 4a on the right and see Section 6.1 in the Supporting Information for more details). We assume that the stacking boundary exists between two adjacent layers of the trilayer sample where the A-stacked region and M-stacked region meet, while the third layer is continuous. The stacking boundary between the AA stacking and the A+M stacking appears in the virtual dark-field images from two of the d' peaks and disappears in the virtual dark-field image from the third d' peak (Figure S14c-e). This indicates that the translation vector $\boldsymbol{\Delta u}$ across the boundary is again along a zigzag direction of the Cr lattice with magnitude $|\boldsymbol{\Delta u}| = \frac{1}{3}a_0$, like all the other stacking boundaries observed in this study.

We then map the strain field at this stacking boundary between AA and A+M stackings. We choose to map the strain field specifically for this case, not only because this boundary is representative of a strain boundary in bi- and tri-layer CrX_3 in terms of the sliding direction and magnitude, but also because the strong presence of six d peaks in the diffraction pattern

corresponding to AA stacking further enhances the signal-to-noise ratio during data analysis using the "Whole Pattern Fitting" (WPF) method (see Experimental Section and Section 6.2 in the Supporting Information).

With one of the primary axes along the direction of the in-plane displacement vector $\boldsymbol{u}$ (which is also the interlayer translation vector $\Delta\boldsymbol{u}$), we observe both tensile and shear strain and a rotation of lattices at the boundary between the two domains with the AA stacking and the A+M stacking, while within the domains with the two stacking sequences there is no considerable strain and rotation. In the strain maps in Figure 4b and c, ε_{xx} represents the tensile or compressive (positive or negative) strain along the x-axis, and ε_{yy} represents the tensile or compressive (positive or negative) strain along the y-axis. The pure shear strain and rotation of lattices are represented by ε_{xy} and θ (Figure 4d and e), respectively. Here, positive (negative) shear strain corresponds to a more obtuse (acute) angle between two deformed lattice vectors, while positive (negative) θ corresponds to a counterclockwise (clockwise) rotation in a right-handed coordinate system. In Figure 4b and c, the ε_{xx} map shows almost no tensile strain, except for a small patch at the bottom of the boundary with maximum magnitude of $\sim 0.30\%$, while the ε_{yy} map shows uniform tensile strain with typical magnitude $\sim 0.40\%$ distributed over the entire boundary except for the bottom of the boundary. Furthermore, we observe a uniform distribution of tensorial shear strain (ε_{xy}) with typical magnitude of $\sim -0.40\%$ and lattice rotation (θ) of $\sim -0.23°$ at the boundary (Figure 4d and e). We also plot the strain map for the two sheets of capping few-layer graphene as shown in Figure S19. Despite some stray strain at a few spots in both few-layer graphene sheets, there is no apparent strain field associated with the $CrCl_3$ boundary. This indicates that the strain we observe at the boundary in the $CrCl_3$ layers is not from the capping few-layer graphene.

With the above strain field analysis, we can obtain a simpler picture of the strain distribution at the boundary by mapping the direction and magnitude of the maximum shear strain γ (Figure 4f, also see Section 6.2 in the Supporting Information). We find that the direction of the maximum shear strain is mainly along the in-plane displacement vector (also the sliding direction between the two stacking sequences) and has magnitude of $0.85 \pm 0.25\%$ with the highest values concentrated at the boundary. This indicates that this boundary is mostly a shear boundary with a small rotation angle reconstruction.[51] We note that the strain field mapping at a stacking boundary between a M-stacking and a M+R stacking in trilayer $CrCl_3$ has also been performed as shown in Figure S20 in supporting information Section 6.3, where challenges of strain analysis at such boundaries are detailed. Future studies are needed to statistically determine which type of strain boundaries (tensile or shear) are more prominent in bilayer and trilayer CrX_3 with different stacking sequences.

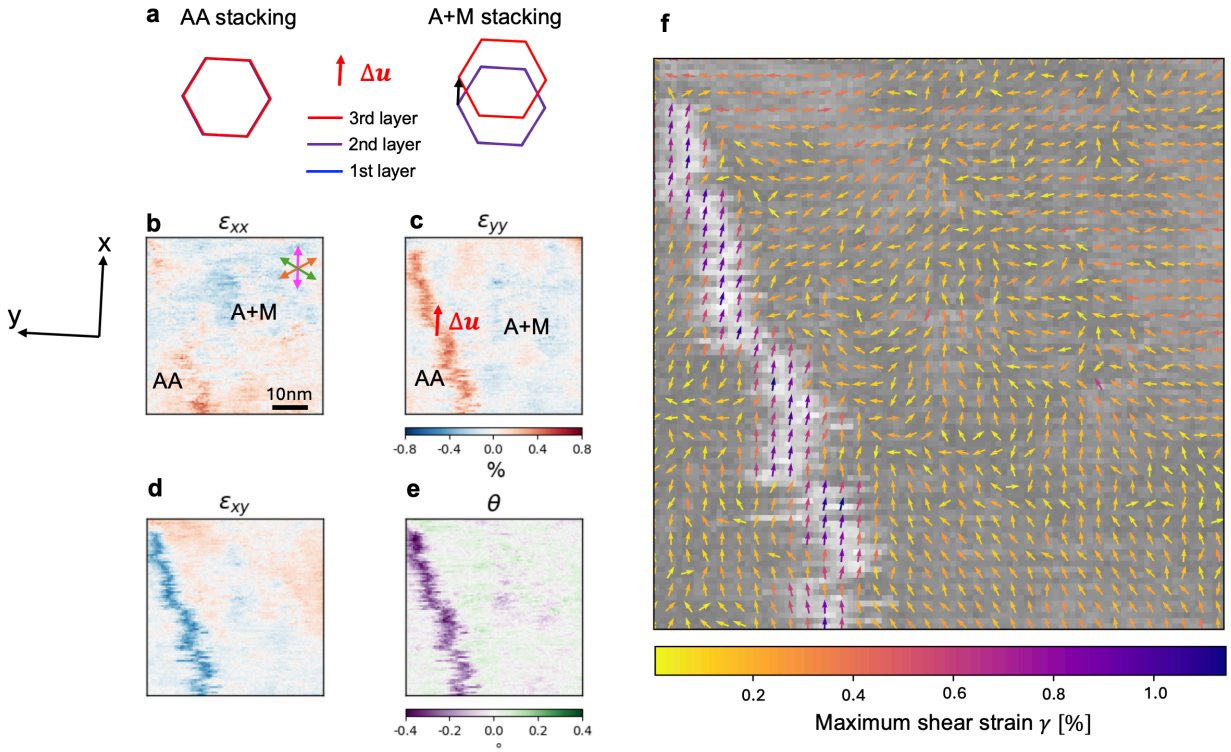

Figure 4: Strain maps at the stacking boundary between a rare AA stacking and a mixture of A and M stacking in a trilayer* $CrCl_3$ *sample. *(a) Schematics of the two stacking sequences that occur at the two sides of the boundary: A+M stacking and AA stacking. In AA-stacked trilayer* $CrCl_3$*, all three layers are overlapped with each other. (b-e) Strain maps based on two-dimensional infinitesimal strain tensor components, showing the normal strain along the x-direction–*ε_{xx}*, the normal strain along the y-direction–*ε_{yy}*, the tensorial shear strain–*ε_{xy}*, and lattice rotation* θ*, respectively. (b)-(e) have the same scale bar. (f) Map of maximum shear strain* γ *distributed at the boundary and in the two domains with the AA stacking and A+M stacking. The direction of the arrows indicates the direction of the maximum shear strain while the color indicates the magnitude of the strain based on the color scale.*

Conclusion

We use 4D-STEM to study stacking configurations in exfoliated bilayer and tri-layer CrX_3 (X=Cl and Br) and observe coexistence of various stacking sequences that correspond to different bulk phases of the CrX_3. We find that stacking boundaries usually occur between two domains with a dominant stacking sequence and a minor stacking sequence, respectively. The dominant stacking sequence in exfoliated bi- and tri-layer $CrCl_3$ is M-stacking (corresponding to the monoclinic phase), but regions usually around tens or hundreds of nm in size with the minor R-stacking (corresponding to the rhombohedral phase) can also occur. DFT calculations confirm that the transition between a dominant stacking sequence and a minor stacking sequence is a preferred slipping path compared to the transition between two variant dominant stacking sequences (e.g. variant M-stackings in $CrCl_3$). Similarly, both dominant R-stacking and minor M-stacking can coexist in exfoliated tri-layer $CrBr_3$ and stacking boundaries are found between these two stacking

sequences. In a rare case, a third stacking sequence–AA stacking, which corresponds to a local minimum in energy is observed in trilayer $CrCl_3$.

We also find the stacking boundaries between two different stacking sequences in bi- and tri-layer CrX_3 (X=Cl and Br) are strain boundaries and prefer to slide along the zigzag directions of the Cr lattice across the boundary. This experimental finding is consistent with DFT calculations. Identifying the preferred direction of the cross-boundary sliding can be leveraged to control the stacking sequence in few-layer CrX_3 during the exfoliation and encapsulation process like the stacking control in few-layer graphene.[12] More specifically, one can align the shear force with the armchair direction of the Cr lattice to avoid undesired sliding of the layers to maximize the area with the dominant stacking sequence at room temperature during the stack assembly process. In our study, rich structural variation especially details of the stacking boundaries between different stacking sequences in exfoliated few-layer CrX_3 is characterized with nanometer resolution. Since magnetic properties of thin CrX_3 depend on stacking orders, our observation sheds light into previous studies that reported sample-to-sample variation in magnetic properties of few-layer CrX_3 probed via macroscale transport or optical methods.

Experimental Section

TEM Sample preparation:

CrX_3 (X=Cl, Br) flakes are exfoliated onto a single crystalline Si (100) wafer with an oxidized layer of 90 nm via scotch tape method from parent single crystals. Graphene sheets are exfoliated in an ambient environment while CrX_3 flakes are exfoliated and stored in a glovebox with a dry, inert gas environment (N_2 99.999%, H_2O < 0.1 ppm, O_2 < 0.1 ppm) to avoid degradation. The thickness of CrX_3 flakes is measured using atomic force microscopy located in the same glovebox, which prevents the sample from any exposure to air or moisture. Top few-layer graphene, a CrX_3

flake, and then bottom few-layer graphene are sequentially picked up from SiO_2/Si substrates onto polyethylene terephthalate (PET) at 63-67°C. The whole stack is then gently stamped down to a TEM grid with holey carbon film (658-300-AU, Ted Pella Inc.), which is then placed in dichloromethane (DCM) for 72-96 hours to dissolve the PET and then rinsed with isopropyl alcohol (IPA) for 3 minutes.

4D-STEM measurements:

4D-STEM is used to characterize few-layer graphene encapsulated CrX_3 and is performed on FEI (now Thermo Fisher Scientific Inc.) TitanX and TEAM I (aberration-corrected Thermo Fisher Scientific Titan 80–300) microscopes operated at 80 keV. Under the TitanX microscope, 4D-STEM datasets are acquired using a Gatan Orius 830 camera. The microscope is configured with the following parameters for data acquisition: an indicated convergence semi-angle of 0.3 mrad, spot size 5, a C2 aperture size of 20 μm, and a STEM camera length of 245 mm. These settings yielded an effective probe size of 4.3 nm (full width at half maximum). Diffraction patterns are recorded over a grid of 60 × 60 beam positions, with a step size of 9.84 nm, covering a total area of 600 nm × 600 nm. Each diffraction pattern is captured using 4 × 4 pixel binning, with an exposure time of 100 ms per pattern. These microscopic conditions yield a total electron dose of $\sim 4 \times 10^3\ e^-/Å^2$. Under the TEAM I microscope, 4D-STEM datasets are acquired using a Gatan K3 direct detection camera. The microscope operated in energy-filtered mode at 80 keV, utilizing a 10-eV slit centered on the zero-loss peak to minimize background signal from inelastic scattering. An indicated convergence semi-angle of 1.7 mrad and a beam current of 68 pA are employed, resulting in an effective probe size of 1.2 nm (full width at half maximum). Diffraction patterns are collected over a 100 × 100 beam position grid with a step size of 0.5 nm, covering a 50 nm × 50 nm area. The K3 camera is operated in full-frame electron-counting mode, with 4×4 pixel

binning applied to each diffraction pattern. Data acquisition is performed at an energy-filtered STEM camera length of 1.3 m, with an exposure time of 13 ms per pattern. These microscopic conditions yield a total electron dose of $\sim 2 \times 10^5\ \mathrm{e}^-/\mathrm{Å}^2$. Virtual dark-field images can be formed by using a virtual aperture to select a diffracted beam (such as one of the d or d' peaks in the CBED patterns) in py4DSTEM. We improve the analysis of 4D-STEM data by using a so-called "Whole Pattern Fitting" (WPF) method implemented in py4DSTEM, a Python based software for 4D-STEM data analysis.[52,53] The advantage of using WPF to analyze 4D-STEM data is that we can extract detailed lattice information (notably lattice spacing for strain mapping) with high precision, even from a 2D material sandwiched between two capping layers.[51,52,54]

DFT calculations:

First-principles DFT calculations were performed using the projector augmented-wave (PAW) approach[55] as implemented in the Vienna ab initio simulation package (VASP). The exchange-correlation energy was approximated with the Perdew–Burke–Ernzerhof (PBE) generalized-gradient approximation (GGA).[56] The plane wave cutoff energy was 520 eV and a Gamma only k-point mesh was used. van der Waals interactions were included via the pairwise D3 dispersion correction with Becke–Johnson damping.[57] To model the stacking of $CrCl_3$, we constructed a 168-atom slab model of a 2×2 Cr_3Cl_6 flake on top of a 4×4 Cr_3Cl_6 substrate with a 15 Å vacuum layer. The lateral dimensions of the slab were fixed at the DFT optimized bulk lattice parameters. All structures were optimized until the energy was converged within 10^{-4} eV per supercell and the forces on each atom were less than 0.01 eV/Å. Spin-polarization was considered in all calculations with high-spin initialization. The slip barriers of the $CrCl_3$ flake between different stacking configurations were calculated using the climbing image nudged elastic band (CI-NEB) method with PBE and vdW corrections. A force convergence criterion of 0.02 eV/Å was used in CI-NEB

calculations. The initial migration path was constructed with 5 linearly interpolated images with the starting and end configurations being the monoclinic or rhombohedral stacking. Structural relaxations were performed for the initial and final states. The diffusion barrier was calculated as $\Delta E = E_{max} - E_{initial}$, where E_{max} is the highest energy along the minimum energy pathway and $E_{initial}$ is the energy at the initial state. The choice of flake glide, rather than periodic sliding, was necessitated by limitations of the NEB method, which restricts spring-connected images from crossing periodic boundaries. Simulations using fully periodic $CrCl_3$ layers led to unphysical bond breaking and unrealistically high energy barriers. To assess edge effects, we also tested a larger supercell with reduced accuracy settings, which yielded quantitatively similar results.

Author contribution

A.Y. conceived of the work and designed the research strategy. H.P.B and K.T. fabricated the samples with the assistance from Z.G., C.G. and B.Z., performed initial TEM characterization and data analysis using SAED under the supervision of A.Y.. H.P.B. and A.Y. carried out 4D-STEM experiments with assistance from K.C.B., S.M.R. and J.C.. H.P.B analyzed 4D-STEM data with the assistance from C.O. and S.Z., and under the supervision of A.Y.. C.O. and S.Z. wrote codes for multislice simulation and 4D-STEM data analysis. W.C. and C.H. performed DFT calculations. J.C.L. provided $CrCl_3$ bulk crystals for initial TEM characterization. A.K.Z. provided instrument support for initial characterization of exfoliated $CrCl_3$ samples on SiO_2/Si substrates. J.V.J provided support for sample fabrication. A.Y., H.P.B, W.C. and K.T. wrote the paper. All authors discussed the paper and commented on the paper.

Acknowledgments

A.Y. acknowledges startup funds provided by UC Santa Cruz. A.Y. and H.P.B. acknowledge funding support from the National Science Foundation under award ID 2235474 and Hellman

Fellows program. This work was partially performed at the Molecular Foundry, Lawrence Berkeley National Laboratory, and was supported by the Department of Energy, Office of Science, Office of Basic Energy Sciences, Scientific User Facilities Division of the U.S. Department of Energy under Contract No. DE-AC02-05CH11231. The authors thank C. Song for instrument support on TEAM 1.0 at the Molecular Foundry, Lawrence Berkeley National Laboratory. J.V.J. acknowledges support from the Army Research Office under contract W911NF-17-1-0473.

Conflict of Interest

The authors declare no conflict of interest.

Supporting information

Additional data analysis and experimental information, including initial optical, AFM, TEM characterizations and thickness measurement, determining stacking sequences in bilayer and trilayer CrX_3, interference theory, comparison between experimental and simulated diffraction patterns, determining the stacking sequences in trilayer $CrCl_3$, observation of different stacking sequences and stacking boundaries in trilayer $CrBr_3$, quantification of area fractions of different stacking sequences around stacking boundaries in few-layer CrX_3, identification of a stacking boundary between AA and A+M stacking, strain maps using Whole Pattern Fitting (WPF), and first-principles DFT calculations.

References

(1) Yacoby, A. Tri and Tri Again. *Nat. Phys.* **2011**, *7* (12), 925–926. https://doi.org/10.1038/nphys2166.
(2) Cao, Y. Rhombohedral Graphene Goes Correlated at Four or Five Layers. *Nat. Nanotechnol.* **2024**, *19* (2), 139–140. https://doi.org/10.1038/s41565-023-01566-1.
(3) Balents, L.; Dean, C. R.; Efetov, D. K.; Young, A. F. Superconductivity and Strong Correlations in Moiré Flat Bands. *Nat. Phys.* **2020**, *16* (7), 725–733. https://doi.org/10.1038/s41567-020-0906-9.
(4) Cao, Y.; Fatemi, V.; Fang, S.; Watanabe, K.; Taniguchi, T.; Kaxiras, E.; Jarillo-Herrero, P. Unconventional Superconductivity in Magic-Angle Graphene Superlattices. *Nature* **2018**, *556* (7699), 43–50. https://doi.org/10.1038/nature26160.
(5) Sharpe, A. L.; Fox, E. J.; Barnard, A. W.; Finney, J.; Watanabe, K.; Taniguchi, T.; Kastner, M. A.; Goldhaber-Gordon, D. Emergent Ferromagnetism near Three-Quarters Filling in Twisted Bilayer Graphene. *Science* **2019**, *365* (6453), 605–608. https://doi.org/10.1126/science.aaw3780.
(6) Lu, X.; Stepanov, P.; Yang, W.; Xie, M.; Aamir, M. A.; Das, I.; Urgell, C.; Watanabe, K.; Taniguchi, T.; Zhang, G.; Bachtold, A.; MacDonald, A. H.; Efetov, D. K. Superconductors,

Orbital Magnets and Correlated States in Magic-Angle Bilayer Graphene. *Nature* **2019**, *574* (7780), 653–657. https://doi.org/10.1038/s41586-019-1695-0.
(7) Yankowitz, M.; Chen, S.; Polshyn, H.; Zhang, Y.; Watanabe, K.; Taniguchi, T.; Graf, D.; Young, A. F.; Dean, C. R. Tuning Superconductivity in Twisted Bilayer Graphene. *Science* **2019**, *363* (6431), 1059–1064. https://doi.org/10.1126/science.aav1910.
(8) Alden, J. S.; Tsen, A. W.; Huang, P. Y.; Hovden, R.; Brown, L.; Park, J.; Muller, D. A.; McEuen, P. L. Strain Solitons and Topological Defects in Bilayer Graphene. *Proc. Natl. Acad. Sci.* **2013**, *110* (28), 11256–11260.
(9) Schweizer, P.; Dolle, C.; Spiecker, E. In Situ Manipulation and Switching of Dislocations in Bilayer Graphene. *Sci. Adv.* **2018**, *4* (8), eaat4712. https://doi.org/10.1126/sciadv.aat4712.
(10) Jiang, L.; Wang, S.; Shi, Z.; Jin, C.; Utama, M. I. B.; Zhao, S.; Shen, Y.-R.; Gao, H.-J.; Zhang, G.; Wang, F. Manipulation of Domain-Wall Solitons in Bi- and Trilayer Graphene. *Nat. Nanotechnol.* **2018**, *13* (3), 204–208. https://doi.org/10.1038/s41565-017-0042-6.
(11) Kim, S.; Annevelink, E.; Han, E.; Yu, J.; Huang, P. Y.; Ertekin, E.; Van Der Zande, A. M. Stochastic Stress Jumps Due to Soliton Dynamics in Two-Dimensional van Der Waals Interfaces. *Nano Lett.* **2020**, *20* (2), 1201–1207. https://doi.org/10.1021/acs.nanolett.9b04619.
(12) Yang, Y.; Zou, Y.-C.; Woods, C. R.; Shi, Y.; Yin, J.; Xu, S.; Ozdemir, S.; Taniguchi, T.; Watanabe, K.; Geim, A. K.; Novoselov, K. S.; Haigh, S. J.; Mishchenko, A. Stacking Order in Graphite Films Controlled by van Der Waals Technology. *Nano Lett.* **2019**, *19* (12), 8526–8532. https://doi.org/10.1021/acs.nanolett.9b03014.
(13) Edelberg, D.; Kumar, H.; Shenoy, V.; Ochoa, H.; Pasupathy, A. N. Tunable Strain Soliton Networks Confine Electrons in van Der Waals Materials. *Nat. Phys.* **2020**, *16* (11), 1097–1102. https://doi.org/10.1038/s41567-020-0953-2.
(14) Sivadas, N.; Okamoto, S.; Xu, X.; Fennie, C. J.; Xiao, D. Stacking-Dependent Magnetism in Bilayer CrI3. *Nano Lett.* **2018**, *18* (12), 7658–7664.
(15) Gibertini, M. Magnetism and Stability of All Primitive Stacking Patterns in Bilayer Chromium Trihalides. *J. Phys. Appl. Phys.* **2020**, *54* (6), 064002. https://doi.org/10.1088/1361-6463/abc2f4.
(16) Gong, C.; Li, L.; Li, Z.; Ji, H.; Stern, A.; Xia, Y.; Cao, T.; Bao, W.; Wang, C.; Wang, Y.; Qiu, Z. Q.; Cava, R. J.; Louie, S. G.; Xia, J.; Zhang, X. Discovery of Intrinsic Ferromagnetism in Two-Dimensional van Der Waals Crystals. *Nature* **2017**, *546* (7657), 265–269. https://doi.org/10.1038/nature22060.
(17) Huang, B.; Clark, G.; Navarro-Moratalla, E.; Klein, D. R.; Cheng, R.; Seyler, K. L.; Zhong, D.; Schmidgall, E.; McGuire, M. A.; Cobden, D. H.; others. Layer-Dependent Ferromagnetism in a van Der Waals Crystal down to the Monolayer Limit. *Nature* **2017**, *546* (7657), 270–270.
(18) Jiang, S.; Li, L.; Wang, Z.; Mak, K. F.; Shan, J. Controlling Magnetism in 2D CrI3 by Electrostatic Doping. *Nat. Nanotechnol.* **2018**, *13* (7), 549–553. https://doi.org/10.1038/s41565-018-0135-x.
(19) Wang, Z.; Zhang, T.; Ding, M.; Dong, B.; Li, Y.; Chen, M.; Li, X.; Huang, J.; Wang, H.; Zhao, X.; Li, Y.; Li, D.; Jia, C.; Sun, L.; Guo, H.; Ye, Y.; Sun, D.; Chen, Y.; Yang, T.; Zhang, J.; Ono, S.; Han, Z.; Zhang, Z. Electric-Field Control of Magnetism in a Few-Layered van Der Waals Ferromagnetic Semiconductor. *Nat. Nanotechnol.* **2018**, *13* (7), 554–559. https://doi.org/10.1038/s41565-018-0186-z.
(20) Jiang, S.; Shan, J.; Mak, K. F. Electric-Field Switching of Two-Dimensional van Der Waals Magnets. *Nat. Mater.* **2018**, *17* (5), 406–410. https://doi.org/10.1038/s41563-018-0040-6.

(21) Huang, B.; Clark, G.; Klein, D. R.; MacNeill, D.; Navarro-Moratalla, E.; Seyler, K. L.; Wilson, N.; McGuire, M. A.; Cobden, D. H.; Xiao, D.; Yao, W.; Jarillo-Herrero, P.; Xu, X. Electrical Control of 2D Magnetism in Bilayer CrI3. *Nat. Nanotechnol.* **2018**, *13* (7), 544–548. https://doi.org/10.1038/s41565-018-0121-3.
(22) Wadley, P.; Howells, B.; Železný, J.; Andrews, C.; Hills, V.; Campion, R. P.; Novák, V.; Olejník, K.; Maccherozzi, F.; Dhesi, S. S.; Martin, S. Y.; Wagner, T.; Wunderlich, J.; Freimuth, F.; Mokrousov, Y.; Kuneš, J.; Chauhan, J. S.; Grzybowski, M. J.; Rushforth, A. W.; Edmonds, K. W.; Gallagher, B. L.; Jungwirth, T. Electrical Switching of an Antiferromagnet. *Science* **2016**, *351* (6273), 587–590. https://doi.org/10.1126/science.aab1031.
(23) Chen, W.; Sun, Z.; Wang, Z.; Gu, L.; Xu, X.; Wu, S.; Gao, C. Direct Observation of van Der Waals Stacking–Dependent Interlayer Magnetism. *Science* **2019**, *366* (6468), 983–987. https://doi.org/10.1126/science.aav1937.
(24) Klein, D. R.; MacNeill, D.; Song, Q.; Larson, D. T.; Fang, S.; Xu, M.; Ribeiro, R. A.; Canfield, P. C.; Kaxiras, E.; Comin, R.; others. Enhancement of Interlayer Exchange in an Ultrathin Two-Dimensional Magnet. *Nat. Phys.* **2019**, *15* (12), 1255–1260.
(25) Kim, H. H.; Yang, B.; Li, S.; Jiang, S.; Jin, C.; Tao, Z.; Nichols, G.; Sfigakis, F.; Zhong, S.; Li, C.; Tian, S.; Cory, D. G.; Miao, G.-X.; Shan, J.; Mak, K. F.; Lei, H.; Sun, K.; Zhao, L.; Tsen, A. W. Evolution of Interlayer and Intralayer Magnetism in Three Atomically Thin Chromium Trihalides. *Proc. Natl. Acad. Sci.* **2019**, *116* (23), 11131–11136. https://doi.org/10.1073/pnas.1902100116.
(26) Wang, Z.; Gutiérrez-Lezama, I.; Ubrig, N.; Kroner, M.; Gibertini, M.; Taniguchi, T.; Watanabe, K.; Imamoğlu, A.; Giannini, E.; Morpurgo, A. F. Very Large Tunneling Magnetoresistance in Layered Magnetic Semiconductor CrI3. *Nat. Commun.* **2018**, *9* (1), 2516. https://doi.org/10.1038/s41467-018-04953-8.
(27) Yao, F.; Multian, V.; Wang, Z.; Ubrig, N.; Teyssier, J.; Wu, F.; Giannini, E.; Gibertini, M.; Gutiérrez-Lezama, I.; Morpurgo, A. F. Multiple Antiferromagnetic Phases and Magnetic Anisotropy in Exfoliated CrBr3 Multilayers. *Nat. Commun.* **2023**, *14* (1), 4969. https://doi.org/10.1038/s41467-023-40723-x.
(28) Zhang, B.; Lu, P.; Tabrizian, R.; Feng, P. X.-L.; Wu, Y. 2D Magnetic Heterostructures: Spintronics and Quantum Future. *Npj Spintron.* **2024**, *2* (1), 6. https://doi.org/10.1038/s44306-024-00011-w.
(29) Ningrum, V. P.; Liu, B.; Wang, W.; Yin, Y.; Cao, Y.; Zha, C.; Xie, H.; Jiang, X.; Sun, Y.; Qin, S.; Chen, X.; Qin, T.; Zhu, C.; Wang, L.; Huang, W. Recent Advances in Two-Dimensional Magnets: Physics and Devices towards Spintronic Applications. *Research* **2020**, *2020*, 1–19. https://doi.org/10.34133/2020/1768918.
(30) Lin, X.; Yang, W.; Wang, K. L.; Zhao, W. Two-Dimensional Spintronics for Low-Power Electronics. *Nat. Electron.* **2019**, *2* (7), 274–283.
(31) Jimenez, V. O.; Kalappattil, V.; Eggers, T.; Bonilla, M.; Kolekar, S.; Huy, P. T.; Batzill, M.; Phan, M.-H. A Magnetic Sensor Using a 2D van Der Waals Ferromagnetic Material. *Sci. Rep.* **2020**, *10* (1), 4789. https://doi.org/10.1038/s41598-020-61798-2.
(32) Papavasileiou, A. V.; Menelaou, M.; Sarkar, K. J.; Sofer, Z.; Polavarapu, L.; Mourdikoudis, S. Ferromagnetic Elements in Two-Dimensional Materials: 2D Magnets and Beyond. *Adv. Funct. Mater.* **2024**, *34* (2), 2309046. https://doi.org/10.1002/adfm.202309046.
(33) Sun, Z.; Yi, Y.; Song, T.; Clark, G.; Huang, B.; Shan, Y.; Wu, S.; Huang, D.; Gao, C.; Chen, Z.; McGuire, M.; Cao, T.; Xiao, D.; Liu, W.-T.; Yao, W.; Xu, X.; Wu, S. Giant Nonreciprocal

Second-Harmonic Generation from Antiferromagnetic Bilayer CrI3. *Nature* **2019**, *572* (7770), 497–501. https://doi.org/10.1038/s41586-019-1445-3.
(34) Morosin, B.; Narath, A. X-Ray Diffraction and Nuclear Quadrupole Resonance Studies of Chromium Trichloride. *J. Chem. Phys.* **1964**, *40* (7), 1958–1967. https://doi.org/10.1063/1.1725428.
(35) McGuire, M. A.; Dixit, H.; Cooper, V. R.; Sales, B. C. Coupling of Crystal Structure and Magnetism in the Layered, Ferromagnetic Insulator CrI $_3$. *Chem. Mater.* **2015**, *27* (2), 612–620. https://doi.org/10.1021/cm504242t.
(36) Wang, Z.; Gutiérrez-Lezama, I.; Dumcenco, D.; Ubrig, N.; Taniguchi, T.; Watanabe, K.; Giannini, E.; Gibertini, M.; Morpurgo, A. F. Magnetization Dependent Tunneling Conductance of Ferromagnetic Barriers. *Nat. Commun.* **2021**, *12* (1), 6659. https://doi.org/10.1038/s41467-021-26973-7.
(37) Ghazaryan, D.; Greenaway, M. T.; Wang, Z.; Guarochico-Moreira, V. H.; Vera-Marun, I. J.; Yin, J.; Liao, Y.; Morozov, S. V.; Kristanovski, O.; Lichtenstein, A. I.; Katsnelson, M. I.; Withers, F.; Mishchenko, A.; Eaves, L.; Geim, A. K.; Novoselov, K. S.; Misra, A. Magnon-Assisted Tunnelling in van Der Waals Heterostructures Based on CrBr3. *Nat. Electron.* **2018**, *1* (6), 344–349. https://doi.org/10.1038/s41928-018-0087-z.
(38) Kim, M.; Kumaravadivel, P.; Birkbeck, J.; Kuang, W.; Xu, S. G.; Hopkinson, D. G.; Knolle, J.; McClarty, P. A.; Berdyugin, A. I.; Ben Shalom, M.; Gorbachev, R. V.; Haigh, S. J.; Liu, S.; Edgar, J. H.; Novoselov, K. S.; Grigorieva, I. V.; Geim, A. K. Micromagnetometry of Two-Dimensional Ferromagnets. *Nat. Electron.* **2019**, *2* (10), 457–463. https://doi.org/10.1038/s41928-019-0302-6.
(39) Meseguer-Sánchez, J.; Popescu, C.; García-Muñoz, J. L.; Luetkens, H.; Taniashvili, G.; Navarro-Moratalla, E.; Guguchia, Z.; Santos, E. J. G. Coexistence of Structural and Magnetic Phases in van Der Waals Magnet CrI3. *Nat. Commun.* **2021**, *12* (1), 6265. https://doi.org/10.1038/s41467-021-26342-4.
(40) Shcherbakov, D.; Stepanov, P.; Weber, D.; Wang, Y.; Hu, J.; Zhu, Y.; Watanabe, K.; Taniguchi, T.; Mao, Z.; Windl, W.; Goldberger, J.; Bockrath, M.; Lau, C. N. Raman Spectroscopy, Photocatalytic Degradation, and Stabilization of Atomically Thin Chromium Tri-Iodide. *Nano Lett.* **2018**, *18* (7), 4214–4219. https://doi.org/10.1021/acs.nanolett.8b01131.
(41) Jang, M.; Lee, S.; Cantos-Prieto, F.; Košić, I.; Li, Y.; McCray, A. R. C.; Jung, M.-H.; Yoon, J.-Y.; Boddapati, L.; Deepak, F. L.; Jeong, H. Y.; Phatak, C. M.; Santos, E. J. G.; Navarro-Moratalla, E.; Kim, K. Direct Observation of Twisted Stacking Domains in the van Der Waals Magnet CrI3. *Nat. Commun.* **2024**, *15* (1), 5925. https://doi.org/10.1038/s41467-024-50314-z.
(42) Sun, Z.; Li, X.; Li, J.; Wei, Y.; Guo, H.; Wang, J. Intrinsic Bitunable Magnetism/Polarity Behavior in 2D Janus Cr2I3Y3 (Y = F, Cl, or Br) Systems. *Npj 2D Mater. Appl.* **2022**, *6* (1), 69. https://doi.org/10.1038/s41699-022-00343-3.
(43) Wang, J.; Ahmadi, Z.; Lujan, D.; Choe, J.; Taniguchi, T.; Watanabe, K.; Li, X.; Shield, J. E.; Hong, X. Physical Vapor Transport Growth of Antiferromagnetic $CrCl_3$ Flakes Down to Monolayer Thickness. *Adv. Sci.* **2023**, *10* (3), 2203548. https://doi.org/10.1002/advs.202203548.
(44) Obraztsova, E. A.; Osadchy, A. V.; Obraztsova, E. D.; Lefrant, S.; Yaminsky, I. V. Statistical Analysis of Atomic Force Microscopy and Raman Spectroscopy Data for Estimation of Graphene Layer Numbers. *Phys. Status Solidi B* **2008**, *245* (10), 2055–2059.

(45) Lai, L.; Irene, E. Limiting Si/SiO2 Interface Roughness Resulting from Thermal Oxidation. *J. Appl. Phys.* **1999**, *86* (3), 1729–1735.
(46) Yao, Y.; Ren, L.; Gao, S.; Li, S. Histogram Method for Reliable Thickness Measurements of Graphene Films Using Atomic Force Microscopy (AFM). *J. Mater. Sci. Technol.* **2017**, *33* (8), 815–820.
(47) Ophus, C. Four-Dimensional Scanning Transmission Electron Microscopy (4D-STEM): From Scanning Nanodiffraction to Ptychography and Beyond. *Microsc. Microanal.* **2019**, *25* (3), 563–582. https://doi.org/10.1017/S1431927619000497.
(48) Held, G. Low-Energy Electron Diffraction. In *Crystallography of Surfaces and Interfaces*; SCHAEFER:METHODS PC 2V O-BK, 2012.
(49) Henkelman, G.; Uberuaga, B. P.; Jónsson, H. A Climbing Image Nudged Elastic Band Method for Finding Saddle Points and Minimum Energy Paths. *J. Chem. Phys.* **2000**, *113* (22), 9901–9904. https://doi.org/10.1063/1.1329672.
(50) Yang, S.; Xu, X.; Han, B.; Gu, P.; Guzman, R.; Song, Y.; Lin, Z.; Gao, P.; Zhou, W.; Yang, J.; others. Controlling the 2D Magnetism of CrBr3 by van Der Waals Stacking Engineering. *J. Am. Chem. Soc.* **2023**, *145* (51), 28184–28190.
(51) Kazmierczak, N. P.; Van Winkle, M.; Ophus, C.; Bustillo, K. C.; Carr, S.; Brown, H. G.; Ciston, J.; Taniguchi, T.; Watanabe, K.; Bediako, D. K. Strain Fields in Twisted Bilayer Graphene. *Nat. Mater.* **2021**, 1–8.
(52) Savitzky, B. H.; Zeltmann, S. E.; Hughes, L. A.; Brown, H. G.; Zhao, S.; Pelz, P. M.; Pekin, T. C.; Barnard, E. S.; Donohue, J.; DaCosta, L. R.; others. py4DSTEM: A Software Package for Four-Dimensional Scanning Transmission Electron Microscopy Data Analysis. *Microsc. Microanal.* **2021**, 1–32.
(53) Zeltmann, S. E.; Bhusal, H. P.; Yan, A.; Ophus, C. Robust Strain Analysis of Complex Heterostructures by Whole Pattern Fitting, 2024.
(54) Zeltmann, S. E.; Müller, A.; Bustillo, K. C.; Savitzky, B.; Hughes, L.; Minor, A. M.; Ophus, C. Patterned Probes for High Precision 4D-STEM Bragg Measurements. *Ultramicroscopy* **2020**, *209*, 112890. https://doi.org/10.1016/j.ultramic.2019.112890.
(55) Blöchl, P. E. Projector Augmented-Wave Method. *Phys. Rev. B* **1994**, *50* (24), 17953–17979. https://doi.org/10.1103/PhysRevB.50.17953.
(56) Perdew, J. P.; Burke, K.; Ernzerhof, M. Generalized Gradient Approximation Made Simple. *Phys. Rev. Lett.* **1996**, *77* (18), 3865–3868. https://doi.org/10.1103/PhysRevLett.77.3865.
(57) Grimme, S.; Ehrlich, S.; Goerigk, L. Effect of the Damping Function in Dispersion Corrected Density Functional Theory. *J. Comput. Chem.* **2011**, *32* (7), 1456–1465. https://doi.org/10.1002/jcc.21759.

For Table of Contents Only